Anisotropic Quantum Corrections for 3-D Finite-Element Monte Carlo Simulations of Nanoscale Multigate Transistors

Muhammad A. Elmessary, Daniel Nagy, Manuel Aldegunde, Jari Lindberg, Wulf G. Dettmer, Djordje Perić, Antonio J. García-Loureiro, and Karol Kalna

***Abstract*— Anisotropic 2-D Schrödinger equation-based quantum corrections dependent on valley orientation are incorporated into a 3-D finite-element Monte Carlo simulation toolbox. The new toolbox is then applied to simulate nanoscale Si Silicon-on-Insulator FinFETs with a gate length of 8.1 nm to study the contributions of conduction valleys to the drive current in various FinFET architectures and channel orientations. The 8.1 nm gate length FinFETs are studied for two cross sections: rectangular-like and triangular-like, and for two channel orientations: ⟨100⟩ and ⟨110⟩. We have found that quantum anisotropy effects play the strongest role in the triangular-like ⟨100⟩ channel device increasing the drain current by ∼13% and slightly decreasing the current by 2% in the rectangular-like ⟨100⟩ channel device. The quantum anisotropy has a negligible effect in any device with the ⟨110⟩ channel orientation.**

***Index Terms*— Anisotropy, Monte Carlo (MC) simulations, Schrödinger quantum corrections (QCs), Silicon-on-Insulator FinFETs.**

I. Introduction

MULTIGATE nonplanar FETs are leading solutions for sub-14 nm technology nodes because of their exceptional electrostatic integrity [1], [2]. These nanoscale device structures possess a very complex 3-D geometry created by the fabrication process flow [3]. The resulting irregular transistor shapes can be precisely described by the 3-D finite-element (FE) method that is essential to determine quantum confinement, which will play a crucial role in carrier density distribution and carrier transport along the device channel [4].

In this paper, we report on anisotropic FE Schrödinger equation-based quantum corrections (QCs) incorporated into in-house 3-D FE Monte Carlo (MC) device toolbox [5], [6]. The MC transport engine has already included anisotropic bandstructure [6]–[8] using **k**-vector transformations [9], but the Schrödinger equation QCs were approximated by isotropic electron effective mass tensor (EMT) [5]. Here, we extend the calibration-free Schrödinger equation QCs into three separate Δ valleys (see Fig. 1) using longitudinal and transverse electron effective masses. The QC approach in the 3-D MC device simulations is more efficient than the multisubband MC [10], [11], especially in 3-D simulations of multigate devices with cross sections in the range of 5–20 nm and at large applied biases when carriers undergo frequent intersubband transitions in addition to intrasubband ones while still delivering the expected predictive power [6], [12]. The developed 3-D FE MC toolbox with anisotropic FE Schrödinger QCs is applied to nanoscale *n*-channel Si Silicon-on-Insulator (SOI) FinFETs with a gate length of 8.1 nm designed following the International Technology Roadmap for Semiconductors (ITRS) specifications [13]. In order to fully exploit the capability of the anisotropic QCs, we consider two FinFETs with different cross sections: 1) rectangular-like [Fig. 2(a)] and 2) triangular-like [14] [Fig. 2(b)]. For each device, we simulate

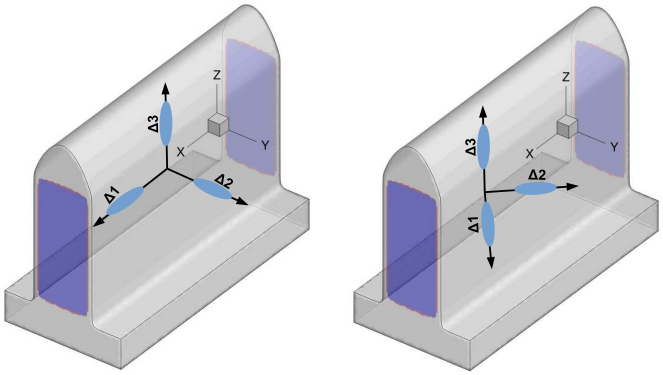

(a) (b)

Fig. 1. Conduction band constant energy ellipsoids along Δ valleys in silicon for (a) ⟨100⟩ and (b) ⟨110⟩ channel orientations. Each of the three ellipsoids is double degenerate.

Manuscript received February 23, 2015; accepted January 12, 2016. Date of publication February 3, 2016; date of current version February 23, 2016. The review of this paper was arranged by Editor J. C. S. Woo. *(Corresponding author: Muhammad A. Elmessary.)*

M. A. Elmessary is with the Electronic Systems Design Centre, College of Engineering, Swansea University, Swansea SA1 8QQ, U.K., and also with the Engineering Mathematics and Physics Department, Faculty of Engineering, Mansoura University, Mansoura 35516, Egypt (e-mail: m.a.a.elmessary.716902@swansea.ac.uk).

D. Nagy and K. Kalna are with the Electronic Systems Design Centre, College of Engineering, Swansea University, Swansea SA1 8QQ, U.K. (e-mail: d.nagy.491828@swansea.ac.uk; k.kalna@swansea.ac.uk).

M. Aldegunde is with the Warwick Centre for Predictive Modelling, School of Engineering, University of Warwick, Coventry CV4 7AL, U.K. (e-mail: m.a.aldegunde-rodriguez@warwick.ac.uk).

J. Lindberg is with the H. H. Wills Physics Laboratory, University of Bristol, Bristol BS8 1TL, U.K. (e-mail: jarilindberg2@gmail.com).

W. G. Dettmer and D. Perić are with the Civil and Computational Engineering Centre, College of Engineering, Swansea University, Swansea SA1 8QQ, U.K. (e-mail: w.g.dettmer@swansea.ac.uk; d.peric@swansea.ac.uk).

A. J. García-Loureiro is with the Centro de Investigación en Tecnoloxáas da Información, Universidade de Santiago de Compostela, Santiago de Compostela 15782, Spain (e-mail: antonio.garcia.loureiro@usc.es).

Color versions of one or more of the figures in this paper are available online at http://ieeexplore.ieee.org.

Digital Object Identifier 10.1109/TED.2016.2519822

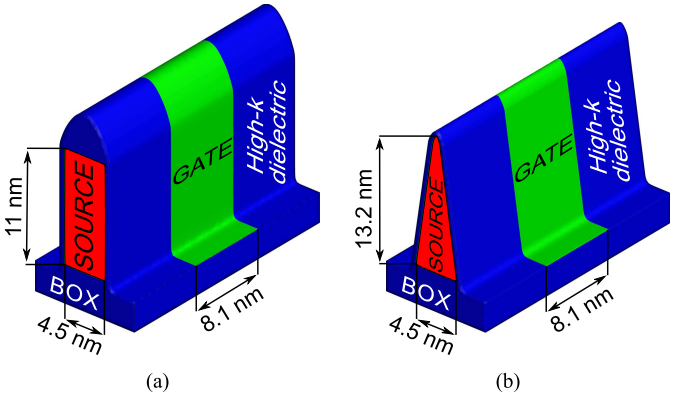

Fig. 2. Schematics of the 8.1-nm gate length n-channel SOI FinFETs with (a) rectangular-like and (b) triangular-like cross sections.

two different channel orientations: 1) the (110) top surface and (100) sidewalls referred to as the ⟨100⟩ channel and 2) the (100) top surface and (110) sidewalls as the ⟨110⟩ channel. While the impact of anisotropy in multigate transistors was investigated in the past [15], this new FE toolbox allows to determine how much improvement in performance can be related to the particular cross section/channel orientation and which cross-sectional dimension is critical to predict the accurate quantitative contribution to the electron transport.

II. 3-D Monte Carlo Simulation Toolbox

The 3-D FE ensemble MC device simulation toolbox uses anisotropic nonparabolic bandstructure for transport [7] with all Si-related electron scattering mechanisms, including interface roughness and ionized impurity scatterings. More details on the 3-D MC transport model can be found in [5], [6], and [16]. The QCs, essential in nanoscale MOSFETs, are incorporated using the solutions of the 2-D FE Schrödinger equation [5] that need no calibration [17]. Initially, the 3-D FE MC simulation toolbox with the 2-D Schrödinger equation-based QCs [5] used an isotropic (scalar) effective mass. This implies that the same quantum potential is seen by all the particles independently of the orientation of valleys neglecting, thus the confinement-induced valley splitting [5], [12].

Here, we extend the 2-D Schrödinger-based QCs incorporating anisotropy by separating contributions according to the valley orientation [18]. The separate QCs for each valley accurately account for quantum confinement in nanoscale nonplanar Si channels, and have diverse effects in various device cross sections and channel orientations.

We start with a brief description of the simulation process shown in the flowchart in Fig. 3. At the beginning, we solve Schrödinger–Poisson equations at equilibrium to obtain initial distribution of particles depending on the valley population. The injection of particles in the source/drain is adjusted using a velocity-weighted Maxwellian distribution proportional to the valley population as well as considering the respective effective mass in the transport direction. The EMT is constructed depending on the valley orientation. In the ⟨100⟩ orientation, the ellipsoid principal axes of Δ valleys

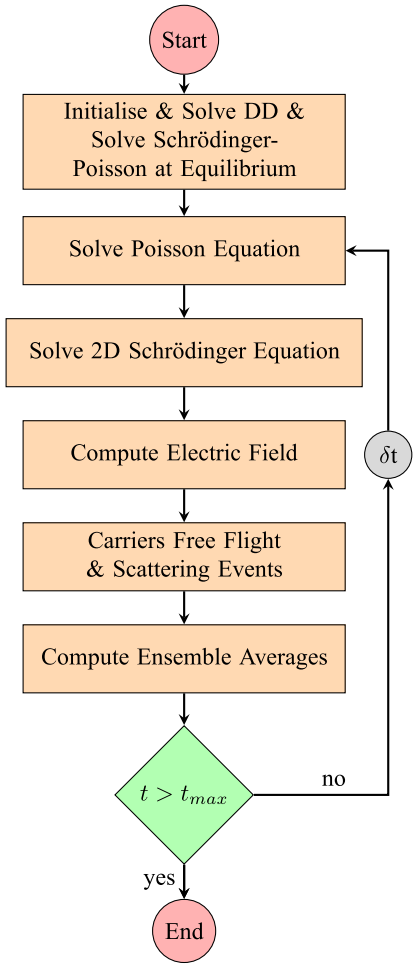

Fig. 3. Flowchart of the 3-D FE MC simulation toolbox.

TABLE I

EMT and Effective Transport Mass of Δ Valleys for ⟨100⟩ and ⟨110⟩ Channel Orientations, Where $1/m^*_{yz} = 0$ and Degeneracy = 2. Wafer Orientation Is [100]

Orientation	Valley	$1/m^*_{yy}$	$1/m^*_{zz}$	m^*_{Tr}
⟨100⟩	Δ1	$1/m_t$	$1/m_t$	m_l
⟨100⟩	Δ2	$1/m_l$	$1/m_t$	m_t
⟨100⟩	Δ3	$1/m_t$	$1/m_l$	m_t
⟨110⟩	Δ1	$(m_t + m_l)/(2m_t m_l)$	$1/m_t$	$(m_t + m_l)/2$
⟨110⟩	Δ2	$(m_t + m_l)/(2m_t m_l)$	$1/m_t$	$(m_t + m_l)/2$
⟨110⟩	Δ3	$1/m_t$	$1/m_l$	m_t

coincide with a device coordinate system. In the ⟨110⟩ orientation, the ellipsoid principal axes are not aligned with the device coordinate system, and therefore, a transformation of coordinates is performed [19]. When the bandgap is large enough ($E_g > 1$ eV), the effective mass approximation accurately represents the complex bandstructure for energies close to the conduction band and, thus, holds well in the case of Si [20]. Table I shows the EMT as well as effective transport mass for the ⟨100⟩ and ⟨110⟩ channel orientations.

The 3-D FE mesh of the simulated device contains predefined 2-D planes perpendicular to the transport direction,

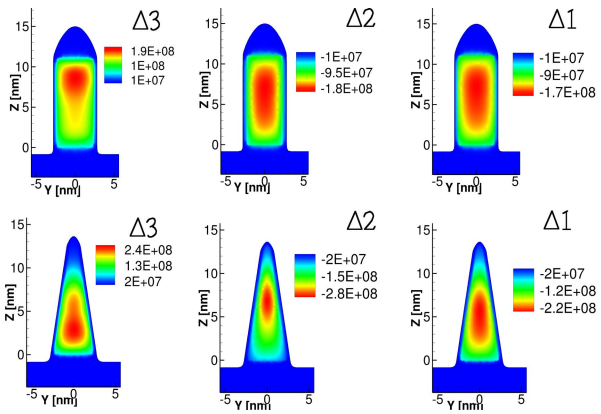

Fig. 4. First wave function for the three Δ valleys (Δ1 in the x-direction, Δ2 in the y-direction, and Δ3 in the z-direction), in the middle of the ⟨100⟩ channel for the rectangular-like (top) and triangular-like (bottom) cross sections at $V_G = 0.8$ V and $V_D = 0.6$ V.

on which we extract the 2-D electrostatic potential to be used in the parabolic 2-D time-independent Schrödinger equation in the form

$$-\frac{\hbar^2}{2}\nabla_\perp \cdot [(\mathbf{m}^*)^{-1} \cdot \nabla_\perp \psi(y,z)] + U(y,z)\psi(y,z) = E\psi(y,z) \tag{1}$$

where E is the energy, $\hbar$ is the reduced Planck's constant, and $(\mathbf{m}^*)^{-1}$ is the inverse EMT with components defined as $(\mathbf{m}^*_{ij})^{-1}$, $i, j = y, z$; $\psi(y,z)$ is the 2-D wave function, and $U(y,z) = -[qV(y,z) + \chi(y,z)]$ is the 2-D potential energy with $\chi(y,z)$ being the electron affinity and q the electron charge [5]. The wave function is assumed to be zero at the outer boundary of the 2-D slice so it penetrates into surrounding oxide. The Schrödinger equation (1) is solved separately for each of the three Δ valleys marked Δ1, Δ2, and Δ3, as shown in Fig. 1. The resulting wave function (Fig. 4) is then used to calculate the 2-D quantum density for each of the three valleys as

$$n_q(y,z) = \frac{2}{\hbar}\sqrt{\frac{2\, m^*_{\mathrm{Tr}}\, k_B T}{\pi}} \sum_i |\psi_i(y,z)|^2 \exp\left[\frac{E_{F_n} - E_i}{k_B T}\right] \tag{2}$$

where m^*_{Tr} is the electron effective transport mass, k_B is the Boltzmann constant, T is the temperature, and E_{F_n} is the quasi-Fermi level. These separate calculations for each valley imply that the effect of valleys splitting with a distinctive population in each of the valleys is considered. The 2-D density is interpolated onto the 3-D simulation domain to obtain a separate QC potential for each valley as [5], [17]

$$V_{\mathrm{qc}}(\mathbf{r}) = \frac{k_B T}{q} \log[n_q(\mathbf{r})/n_{\mathrm{ien}}(\mathbf{r})] - V(\mathbf{r}) + \phi_n(\mathbf{r}) \tag{3}$$

where $n_{\mathrm{ien}}(\mathbf{r})$ is the effective intrinsic carrier concentration of electrons and holes and ϕ_n is the quasi-Fermi potential for electrons. Finally, particles are moved in the quantum-corrected potential of the respective valley according to

$$\frac{d\mathbf{k}}{dt} = \frac{q}{\hbar}\nabla[V(\mathbf{r}) + V_{\mathrm{qc}}(\mathbf{r}))] \tag{4}$$

where t denotes time and $\mathbf{k}$ is the wave vector of the particle.

TABLE II

SUBTHRESHOLD CHARACTERISTICS AT DRAIN BIASES OF 0.05 V (LOW) AND 0.6 V (HIGH), AND DRIVE CURRENT FOR RECTANGULAR AND TRIANGULAR FinFETs COMPARING RESULTS FROM ISOTROPIC (ISO) AND ANISOTROPIC (ANISO) SIMULATIONS

Method	FinFET	Rectangular		Triangular	
		iso	aniso	iso	aniso
MC	V_T [V]	0.25	0.25	0.25	0.25
DD	SS_{LOW} [mV/dec]	72		67	
DD	SS_{HIGH} [mV/dec]	74		68	
MC	$DIBL_{\langle 100\rangle}$ [mV/V]	82	76	70	48
MC	$DIBL_{\langle 110\rangle}$ [mV/V]	84	77	77	51
MC	$I_{\langle 100\rangle}$ [μA/μm]	2128	2075	1537	1667
MC	$I_{\langle 110\rangle}$ [μA/μm]	1766	1728	1258	1251

III. APPLICATION TO NANOSCALED Si SOI FinFETs

The developed 3-D FE MC device simulation toolbox with anisotropic 2-D Schrödinger-based QCs is then employed to study the performance of sub-10 nm gate length Si SOI FinFETs designed according to ITRS specifications [13] with two cross sections (see Fig. 2) and two channel orientations. Thanks to the FE simulation domains with 21 slices distributed along the transport direction for the 2-D Schrödinger-based QCs, the triangular-like and rectangular-like device geometries accurately follow realistic transistor shapes, including rounded corners due to etching processes used in their fabrication. These 8.1-nm gate length multigate FinFETs have the same channel perimeter of 26.5 nm giving an area of 49.5/29.6 nm^2 for the rectangular-like/triangular-like cross section, a high-K dielectric gate-stack with an equivalent oxide thickness of 0.55 nm, and a Gaussian n-type doping in the source/drain using a standard deviation (σ_x) of 2.61 nm [6]. To study the subthreshold slope (SS) (see Table II), we use a 3-D FE drift-diffusion transport model [6], because the ensemble MC is too noisy to accurately calculate very small currents and the source-to-drain tunneling is relatively small in these devices [12].

Figs. 5 and 6 show the I_D–V_G characteristics on logarithmic and linear scales at low and high drain biases of 0.05 and 0.6 V for the 8.1-nm gate length triangular-like and rectangular-like FinFETs, respectively, with the ⟨100⟩ and ⟨110⟩ channel orientations. The drain current is normalized to the gate perimeter (see Fig. 2). The drain current at $V_G = 0$ V is very small and becomes visibly affected by statistical noise and numerical errors inherent to the MC technique [21]. Both triangular-like and rectangular-like devices deliver a higher current for the ⟨100⟩ channel orientation than for the ⟨110⟩ one at both low and high drain biases due to higher electron mobility in the ⟨100⟩ crystallographic orientation in the bulk Si despite that confinement changes the carrier transport to low-dimensional diminishing the difference. An important comparison is the difference of 20% and 33% for the rectangular and triangular FinFET, respectively, between the drive current of ⟨100⟩ and ⟨110⟩ orientations for the 8.1-nm gate length multigate transistors.

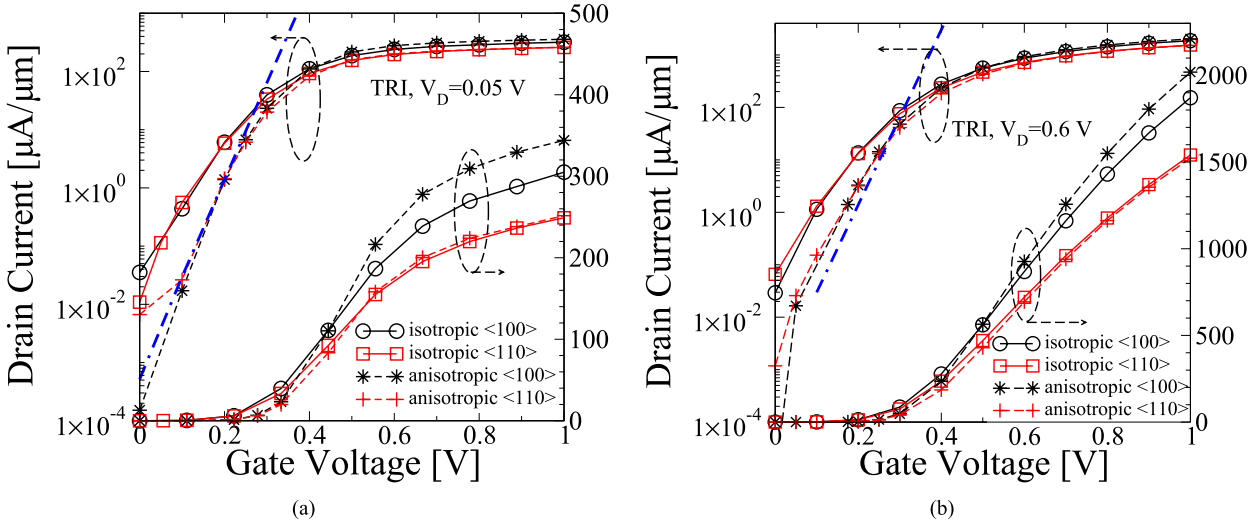

Fig. 5. I_D–V_G characteristics at (a) $V_D = 0.05$ V and (b) $V_D = 0.6$ V for the triangular (TRI) shape FinFET with the ⟨100⟩ and ⟨110⟩ channel orientations showing the effect of the anisotropic QCs (3-D MC). The blue dashed line segment of 60-mV/decade slope shows how well the gate controls the channel.

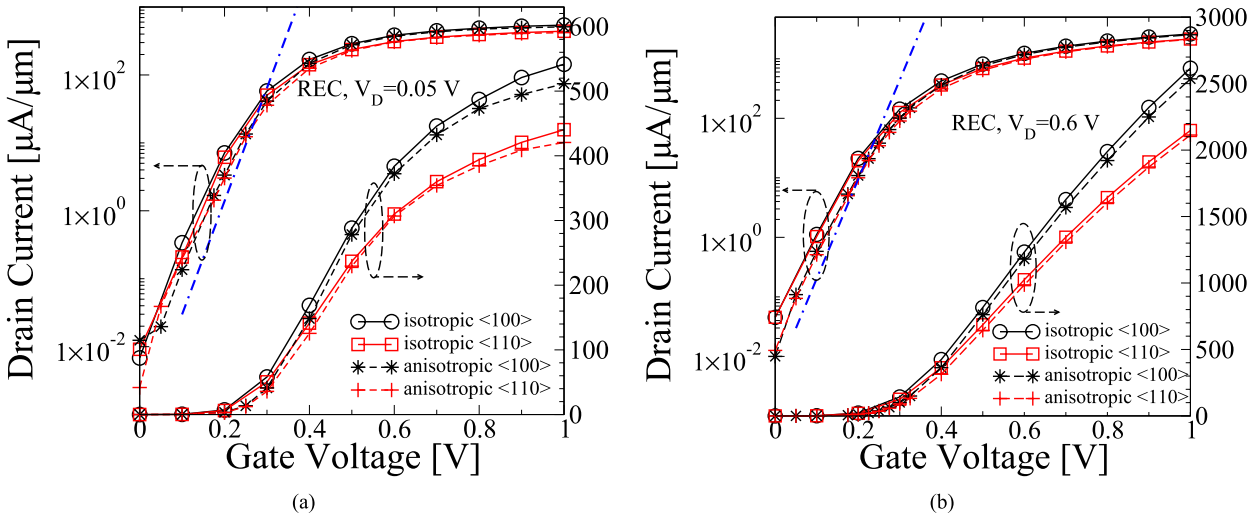

Fig. 6. I_D–V_G characteristics at (a) $V_D = 0.05$ V and (b) $V_D = 0.6$ V for the rectangular (REC) shape FinFET with the ⟨100⟩ and ⟨110⟩ channel orientations showing the effect of the anisotropic QCs (3-D MC). The blue dashed line segment of 60-mV/decade slope shows how well the gate controls the channel.

This difference is only between 10% and 12% for the devices with the gate lengths of 12.8 and 10.7 nm, respectively [12]. Note that for manufacturing, the ⟨110⟩ orientation is preferred, because it is largely beneficial to the hole mobility in p-type transistors assuming that the difference between the ⟨100⟩ and ⟨110⟩ orientations drive current is small.

Table II shows electrostatic integrity characteristics for rectangular-like and triangular-like FinFETs illustrating the effect of anisotropic QC against isotropic QC. The threshold voltage (V_T) for each device variant is very close to 0.25 V. The triangular-like shapes exhibit a better SS and drain-induced barrier lowering than rectangular-like ones thanks to a better confinement of the channel density (see Fig. 11). The drive currents for both devices are a bit reduced with anisotropic QCs, except for the triangular-like device in the ⟨100⟩ channel orientation.

Fig. 5(a) and (b) shows the I_D–V_G characteristics for the triangular-like FinFET at low and high drain biases of 0.05 and 0.6 V, respectively, for both orientations comparing the anisotropic QCs against the isotropic one. In the ⟨100⟩ orientation, the ON-current is increased by 13% and 9% at low and high drain biases, respectively, while in the ⟨110⟩ orientation, the ON-current is very similar with isotropic and anisotropic QC at both biases. In addition, the anisotropic simulations give better SS as indicated by the blue dashed line segment of 60-mV/decade slope. The same comparison of I_D–V_G characteristics but for the rectangular-like FinFET is shown in Fig. 6(a) and (b). The current is reduced only by 2% when using more realistic anisotropic QCs at both low and high drain biases in contrast to the triangular-like shape transistors, which have a stronger confinement and a better gate control over the channel.

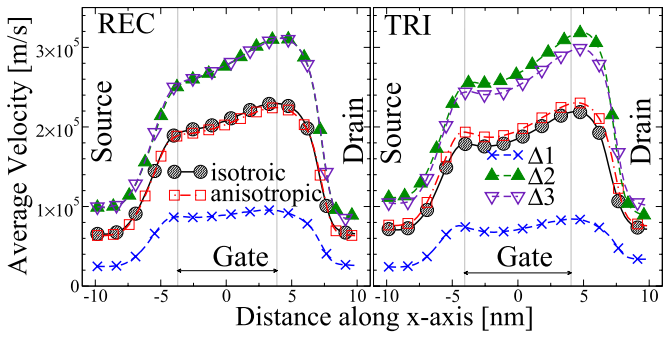

Fig. 7. Average electron velocity along the ⟨100⟩ channel at $V_G = 0.8$ V and $V_D = 0.6$ V for the 8.1-nm gate length rectangular (left) and triangular (right) FinFETs (3-D MC). The zero is set in the middle of the gate.

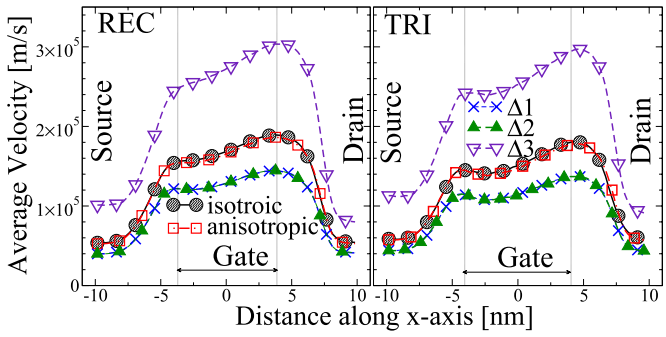

Fig. 8. Average electron velocity along the ⟨110⟩ channel at $V_G = 0.8$ V and $V_D = 0.6$ V for the 8.1-nm gate length rectangular (left) and triangular (right) FinFETs (3-D MC). The zero is set in the middle of the gate.

Figs. 7 and 8 compare the average electron velocity at $V_G = 0.8$ V and $V_D = 0.6$ V for the rectangular-like and triangular-like FinFETs along the ⟨100⟩ and ⟨110⟩ channel orientations, respectively, along with the average velocity in the three silicon valleys Δ1, Δ2, and Δ3. Overall, electrons are accelerated by fringe electric fields when entering the effective channel under gate control. The acceleration is less pronounced under the gate due to enhanced phonon scattering at large kinetic energy. The velocity starts to saturate at the beginning of the gate due to an enhanced interface roughness and phonon scattering, especially, in the triangular device. Finally, it declines at the heavily doped drain due to a strong ionized impurity scattering coupled with phonon emission [7].

When using the anisotropic QC, the overall (sum of contributions from the three valleys) average electron velocity becomes slightly lower in both devices compared with the average velocity obtained from the simulations with isotropic QC, except for the triangular-like device in the ⟨100⟩ channel. In the ⟨100⟩ channel, the Δ1 velocity is the smallest in both device shapes, because the heaviest mass lies in the transport direction and a lighter mass along the confinement direction. The Δ2 and Δ3 velocities are equal in the rectangular-like device because of the shape symmetry. In the triangular-like ⟨100⟩ channel, the Δ2 velocity is larger than the Δ3 velocity, because the quantum confinement along Δ2 is the strongest. In the ⟨110⟩ channel, the situation is opposite with the Δ3 velocity being the largest in both the device shapes, because it has the lightest effective transport

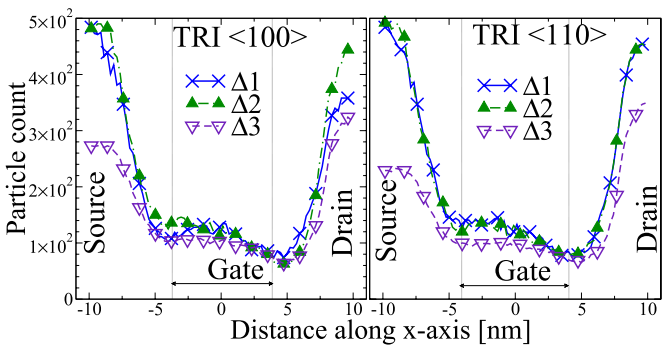

Fig. 9. Average valley population (3-D MC) along the ⟨100⟩ (left) and ⟨110⟩ (right) channel orientations of the 8.1-nm gate length triangular-like FinFETs at $V_G = 0.8$ V and $V_D = 0.6$ V. The zero is set in the middle of the channel.

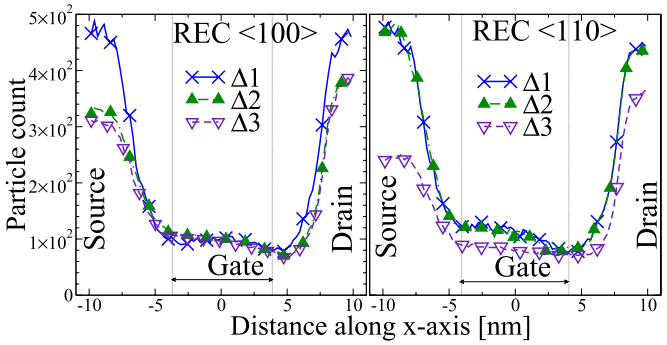

Fig. 10. Average valley population (3-D MC) along the ⟨100⟩ (left) and ⟨110⟩ (right) channel orientations of the 8.1-nm gate length rectangular-like FinFETs at $V_G = 0.8$ V and $V_D = 0.6$ V. The zero is set in the middle of the channel.

mass. The Δ1 and Δ2 velocities are equal, because they have equal effective transport masses (Table I).

Figs. 9 and 10 compare the average valley population along the ⟨100⟩ and ⟨110⟩ channel orientations at $V_G = 0.8$ V and $V_D = 0.6$ V for the triangular and rectangular FinFETs, respectively, using the anisotropic QC. In the ⟨100⟩ orientation, the Δ1 valley is the most populated in the rectangular-like FinFET [Fig. 10 (left)]. Although the Δ2 and Δ3 valleys have the same effective transport mass, the same population occurs only for the rectangular FinFET. In the triangular FinFET [Fig. 9 (left)], the Δ2 valley is more populated than the Δ1, because it lies in a strongly confined y-direction that gives, along with the velocity profile, more current in the ⟨100⟩ triangular device. In the ⟨110⟩ orientation [Figs. 9 and 10 (right)], the Δ3 valley with the smallest effective transport mass has the smallest population in both devices, while the Δ1 and Δ2 valleys are equally populated.

Fig. 11(a) and (b) shows the average electron density cross sections in the middle of the channel for both rectangular and triangular devices, respectively, at $V_G = 0.8$ V and $V_D = 0.6$ V. Note that a different scale for each device is used to show the contrast between high and low areas of density. In both devices, there is volume inversion. In the rectangular device [Fig. 11(a)], the electron density is distributed mostly at the top and the bottom. The density in the triangular device [Fig. 11(b)] is much larger and distributed toward the narrow top due to a stronger confinement.

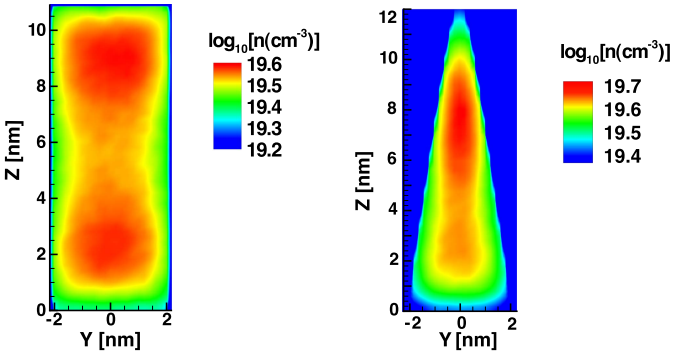

(a) (b)

Fig. 11. Electron density in (a) rectangular-like and (b) triangular-like cross sections at the middle of the channel of 8.1-nm gate length and ⟨100⟩ channel FinFET at $V_G = 0.8$ V and $V_D = 0.6$ V (3-D MC—anisotropic QCs).

IV. Conclusion

A new anisotropic QC using the solutions of 2-D FE Schrödinger equation on the slices along the channel of multigate transistors has been incorporated into the 3-D FE MC device toolbox [6]. The new 3-D FE MC device toolbox with the anisotropic QCs accounting for valley orientation has been then applied for a study of quantum anisotropy effects in the 8.1-nm gate length SOI FinFETs with the ⟨100⟩ and ⟨110⟩ channel orientations comparing rectangular-like and triangular-like cross sections. These two channel orientations and two cross sections allowed us to explore the significance of quantum confinement anisotropy in nanoscale multigate transistors. These findings elevate the triangular-like shape multigate transistors for sub-10-nm technology over the rectangular-like ones and point out loss of more than 30% of the drive current in the ⟨110⟩ channel transistors preferred for the integration into CMOS.

Acknowledgment

The authors would like to thank the EPSRC (UK) for support (grant EP/I010084/).

References

[1] J.-P. Colinge, Ed., *FinFETs and Other Multi-Gate Transistors*. New York, NY, USA: Springer-Verlag, 2008.
[2] T. B. Hook, "Fully depleted devices for designers: FDSOI and FinFETs," in *Proc. IEEE Custom Integr. Circuits Conf.*, Sep. 2012, pp. 1–7.
[3] Y. Liu *et al.*, "Advanced FinFET CMOS technology: TiN-gate, fin-height control and asymmetric gate insulator thickness 4T-FinFETs," in *IEDM Tech. Dig.*, Dec. 2006, pp. 1–4.
[4] A. Ghetti, G. Carnevale, and D. Rideau, "Coupled mechanical and 3-D Monte Carlo simulation of silicon nanowire MOSFETs," *IEEE Trans. Nanotechnol.*, vol. 6, no. 6, pp. 659–666, Nov. 2007.
[5] J. Lindberg *et al.*, "Quantum corrections based on the 2-D Schrödinger equation for 3-D finite element Monte Carlo simulations of nanoscaled FinFETs," *IEEE Trans. Electron Devices*, vol. 61, no. 2, pp. 423–429, Feb. 2014.
[6] M. Aldegunde, A. J. García-Loureiro, and K. Kalna, "3D finite element Monte Carlo simulations of multigate nanoscale transistors," *IEEE Trans. Electron Devices*, vol. 60, no. 5, pp. 1561–1567, May 2013.
[7] A. Islam, B. Benbakhti, and K. Kalna, "Monte Carlo study of ultimate channel scaling in Si and $In_{0.3}Ga_{0.7}As$ bulk MOSFETs," *IEEE Trans. Nanotechnol.*, vol. 10, no. 6, pp. 1424–1432, Nov. 2011.
[8] K. Kalna, N. Seoane, A. J. García-Loureiro, I. G. Thayne, and A. Asenov, "Benchmarking of scaled InGaAs implant-free nanoMOSFETs," *IEEE Trans. Electron Devices*, vol. 55, no. 9, pp. 2297–2306, Sep. 2008.
[9] D. Esseni, P. Palestri, and L. Selmi, *Nanoscale MOS Transistors: Semi-Classical Transport and Applications*. Cambridge, U.K.: Cambridge Univ. Press, 2011.
[10] L. Lucci, P. Palestri, D. Esseni, L. Bergagnini, and L. Selmi, "Multisubband Monte Carlo study of transport, quantization, and electron-gas degeneration in ultrathin SOI n-MOSFETs," *IEEE Trans. Electron Devices*, vol. 54, no. 5, pp. 1156–1164, May 2007.
[11] D. Lizzit, D. Esseni, P. Palestri, P. Osgnach, and L. Selmi, "Performance benchmarking and effective channel length for nanoscale InAs, $In_{0.53}Ga_{0.47}As$, and sSi n-MOSFETs," *IEEE Trans. Electron Devices*, vol. 61, no. 6, pp. 2027–2034, Jun. 2014.
[12] D. Nagy *et al.*, "3-D finite element Monte Carlo simulations of scaled Si SOI FinFET with different cross sections," *IEEE Trans. Nanotechnol.*, vol. 14, no. 1, pp. 93–100, Jan. 2015.
[13] ITRS. (2012). *International Technology Roadmap for Semiconductors*. [Online]. Available: http://www.itrs.net/Links/2012ITRS/Home2012.htm
[14] C. Auth *et al.*, "A 22 nm high performance and low-power CMOS technology featuring fully-depleted tri-gate transistors, self-aligned contacts and high density MIM capacitors," in *VLSI Symp. Tech. Dig.*, 2012, pp. 131–132.
[15] K.-M. Liu, L. F. Register, and S. K. Banerjee, "Quantum transport simulation of strain and orientation effects in sub-20 nm silicon-on-insulator FinFETs," *IEEE Trans. Electron Devices*, vol. 58, no. 1, pp. 4–10, Jan. 2011.
[16] M. Aldegunde, N. Seoane, A. J. García-Loureiro, and K. Kalna, "Reduction of the self-forces in Monte Carlo simulations of semiconductor devices on unstructured meshes," *Comput. Phys. Commun.*, vol. 181, no. 1, pp. 24–34, Jan. 2010.
[17] B. Winstead and U. Ravaioli, "A quantum correction based on Schrödinger equation applied to Monte Carlo device simulation," *IEEE Trans. Electron Devices*, vol. 50, no. 2, pp. 440–446, Feb. 2003.
[18] C. Sampedro-Matarín, F. Gámiz, A. Godoy, and F. J. G. Ruiz, "The multivalley effective conduction band-edge method for Monte Carlo simulation of nanoscale structures," *IEEE Trans. Electron Devices*, vol. 53, no. 11, pp. 2703–2710, Nov. 2006.
[19] A. Rahman, M. S. Lundstrom, and A. W. Ghosh, "Generalized effective-mass approach for *n*-type metal-oxide-semiconductor field-effect transistors on arbitrarily oriented wafers," *J. Appl. Phys.*, vol. 97, no. 5, p. 053702, 2005.
[20] M. Luisier, M. Lundstrom, D. A. Antoniadis, and J. Bokor, "Ultimate device scaling: Intrinsic performance comparisons of carbon-based, InGaAs, and Si field-effect transistors for 5 nm gate length," in *Proc. Int. Electron. Devices Meeting*, Dec. 2011, pp. 11.2.1–11.2.4.
[21] C. Moglestue, *Monte Carlo Simulation of Semiconductor Devices*. London, U.K.: Chapman & Hall, 1993.

Muhammad A. Elmessary received the B.Sc. (Hons.) degree in computer and systems engineering and the M.Sc. degree in engineering physics from Mansoura University, Mansoura, Egypt, in 2004 and 2010, respectively. He is currently pursuing the Ph.D. degree with Swansea University, Swansea, U.K.

His current research interests include nanoscale device simulation using the 3-D finite-element Monte Carlo method.

Daniel Nagy received the M.Res. degree in nanoscience to nanotechnology from Swansea University, Swansea, U.K., in 2013, where he is currently pursuing the Ph.D. degree in electronic and electrical engineering.

His current research interests include electronic transport in modern nanoscaled FinFET devices and their modeling and simulation using the Monte Carlo approach.

Manuel Aldegunde received the Ph.D. degree from the University of Santiago de Compostela, Santiago de Compostela, Spain, in 2009.

He is currently a Research Fellow with the Warwick Centre for Predictive Modeling, University of Warwick, Coventry, U.K. His current research interests include simulation of nanoscale MOSFETs and uncertainty quantification and propagation in materials simulations using density functional theory.

Jari Lindberg received the D.Sc.(Tech.) degree from the Helsinki University of Technology, Espoo, Finland, in 2007.

He was a Post-Doctoral Research Assistant with Swansea University, Swansea, U.K., and the University of Bristol, Bristol, U.K.

Wulf G. Dettmer received the Ph.D. degree from Swansea University, Swansea, U.K., in 2004.

He is currently an Associate Professor with the Civil and Computational Engineering Research Centre, College of Engineering, Swansea University.

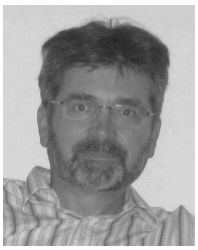

Djordje Perić received the Ph.D. and D.Sc. degrees from the University of Wales, Swansea, U.K., in 1992 and 2000, respectively.

He is currently a Professor and the Programme Director of Civil Engineering with the College of Engineering, Swansea University, Swansea.

Antonio J. García-Loureiro received the Ph.D. degree from the University of Santiago de Compostela, Santiago de Compostela, Spain, in 1999.

He is currently an Associate Professor and the Head with the Department of Electronics and Computer Science, University of Santiago de Compostela.

Karol Kalna received the M.Sc. (Hons.) and Ph.D. degrees from Comenius University, Bratislava, Slovakia, in 1990 and 1998, respectively.

He is currently an Associate Professor with the College of Engineering, Swansea University, Swansea, U.K. In 2010, he became a Senior Lecturer, establishing his own Nanoelectronics Device Simulation Group. He has 72 peer-reviewed papers and 16 invited talks.